Electronic Supplementary Information for

Solution-processable organic semiconductors with over 220 °C glass transition temperature: manipulating morphology using a helical polycyclic heteroaromatic motif

Lingyi Fang, Yuyan Zhang, Yaohang Cai, Jing Zhang, Yuefang Wei, Yi Yuan* and Peng Wang*

State Key Laboratory of Silicon and Advanced Semiconductor Materials, Department of Chemistry, Zhejiang University, Hangzhou 310030, China.

_____

* Corresponding authors.

E-mail addresses: yyuan@zju.edu.cn, pw2015@zju.edu.cn.

1 Experimental section

1.1 Reagents and materials

Sodium hydride (NaH, 60% dispersion in mineral oil, Energy Chemical), iodomethane (99.5%, Energy Chemical), *N*-bromosuccinimide (NBS, 98%, Energy Chemical), sodium sulfite (Na_2SO_3, 98%, Energy Chemical), palladium diacetate (Pd(OAc)$_2$, 99%, Energy Chemical), tris(*o*-tolyl)phosphine (P(*o*-tolyl)$_3$, 98%, Energy Chemical), pivalic acid (PivOH, 99%, Energy Chemical), potassium carbonate (K_2CO_3, 99%, Energy Chemical), benzocyclobutene (BCB, 98%, Energy Chemical), tin oxide colloid precursor (SnO_2, 15% in H_2O colloidal dispersion, Alfa Aesar), lead iodide (PbI$_2$, 99.99%, TCI), rubidium chloride (RbCl, 99.9%, 3A Chemicals), formamidinium iodide (FAI, 99.0%, Greatcell Solar), methylammonium chloride (MACl, $\geq$ 99.5%, Xi'an Polymer Light Technology Corp.), hexakis(methoxymethyl)melamine (HMMM, 98%, TCI), 4-*tert*-butylpyridine (TBP, 96%, Sigma-Aldrich), $N^2,N^2,N^{2'},N^{2'},N^7,N^7,N^{7'},N^{7'}$-octakis(4-methoxyphenyl)-9,9'-spirobi[fluorene]-2,2',7,7'-tetraamine (spiro-OMeTAD, 99.8%, Xi'an Polymer Light Technology Corp.), 1-ethyl-3-methylimidazolium bis(trifluoromethylsulfonyl)imide (EMITFSI, 98%, Energy Chemical), bis(pentamethylcyclopentadienyl)iron (DMFc, 97%, Energy Chemical), and all solvents were purchased from commercial sources and employed without additional purification.

1.2 General instrumentation

Nuclear magnetic resonance (NMR) spectra were acquired using the AVANCE III 400 NMR spectrometer (Bruker) or the DD2-600 NMR spectrometer (Agilent). High-resolution mass spectra (HR-MS) were obtained employing the Ultraflex matrix-assisted laser desorption/ionization time of flight system (Bruker) or the 6545 LC/Q-TOF system (Agilent). Attenuated total reflection-Fourier transform infrared (ATR-FTIR) spectra were collected using the Vector 22 FTIR spectrometer (Bruker). Melting points were determined through utilization of the WRS-1B automatic digital melting point apparatus (Shanghai INESA Physico-Optical Instrument). Elemental analyses for carbon, hydrogen, and nitrogen content were conducted using the Vario Micro cube element analyzer (Elementar Analysensysteme GmbH). Differential scanning calorimetry (DSC) measurements were carried out utilizing the DSC Q100 V9.7 Build 291 (TA) instrument at a heating rate of 10 °C min^{-1} under a flowing nitrogen atmosphere. Cyclic voltammetry (CV) measurements were performed on the CHI660C electrochemical workstation (CH Instruments) using a three-electrode electrolytic cell, consisting of a glassy carbon working electrode, a platinum foil counter electrode, and an Ag/AgCl (sat. KCl) reference electrode. The supporting electrolyte used was 0.1 M EMITFSI in THF solution. Static photoluminescence spectroscopy and time-correlated single photon counting measurements were conducted utilizing the Life-Spec-II fluorescence spectrometer (Edinburgh). Femtosecond fluorescence kinetic traces were captured employing the time-resolved fluorescence

spectrometer (Halcyone Fire, Ultrafast). Water contact angles were assessed utilizing the DropMeter™ A-100P contact angle meter from Maist Co. Ltd. XRD patterns were obtained utilizing the SmartLab diffractometer (Rigaku), operated at 7200 W power (40 kV, 180 mA), with Cu Kα radiation (λ=0.15418 nm). Ultraviolet-visible (UV-Vis) absorption spectra were acquired using the Cary 8454 spectrophotometer (Agilent).

1.3   Synthesis

2,9,16-Tribromo-7,14,21-trimethyl-14,21-dihydro-7*H*-benzo[*g*]benzo[4,5]indolo[3,2-*a*]benzo[4,5]indolo[3,2-*c*]carbazole,[1]   12,19-dihydro-5*H*-benzo[*i*]benzo[6,7]indolo[3,2-*a*]benzo[6,7]indolo[3,2-*c*]carbazole,[2]   4-(2,3-dihydrothieno[3,4-*b*][1,4]dioxin-5-yl)-*N*,*N*-bis(4-methoxyphenyl)aniline (ETPA),[3] and 4-*tert*-butylpyridinium bis(trifluoromethanesulfonyl)imide (TBPHTFSI)[4] were synthesized following established protocols from the literature. New compounds were prepared as follows.

1.3.1   4,4',4''-((7,14,21-Trimethyl-14,21-dihydro-7*H*-benzo[*g*]benzo[4,5]indolo[3,2-*a*]benzo[4,5]indolo[3,2-*c*]carbazole-2,9,16-triyl)tris(2,3-dihydrothieno[3,4-*b*][1,4]dioxine-7,5-diyl))tris(*N*,*N*-bis(4-methoxyphenyl)aniline) (TBTAT-A-C1-e3)

In a dry 500 mL round-bottom flask, TBTAT-A-C1 (2.6 g, 3.4 mmol), ETPA (2.5 g, 5.7 mmol), Pd(OAc)$_2$ (51.2 mg, 0.2 mmol), P(*o*-tolyl)$_3$ (138.8 mg, 0.5 mmol), K$_2$CO$_3$ (4.1 g, 30 mmol), PivOH (131.0 mg, 1.3 mmol), and *N*,*N*-dimethylformamide (250 mL) were combined. The reaction mixture was stirred under an argon atmosphere at 150 °C for 24 hours. After cooling to room temperature, the solvent was evaporated under vacuum. To the residue, 250 mL of dichloromethane was added, and the organic phase was washed three times with deionized water. Subsequent removal of the organic solvent under vacuum, followed by purification on silica gel through column chromatography (using a THF/petroleum ether mixture, *v/v*, 1/2), yielded the yellow solid TBTAT-A-C1-e3 (5.3 g) in an 84% yield. Melting point: > 300 °C. ^{1}H NMR (600 MHz, THF-d_8) δ: 9.04–8.66 (m, 3H), 8.22 (d, *J* = 5.4 Hz, 3H), 7.98 (s, 3H), 7.55 (d, *J* = 4.5 Hz, 9H), 7.41–7.35 (m, 3H), 7.01 (d, *J* = 7.1 Hz, 12H), 6.89 (d, *J* = 7.3 Hz, 6H), 6.82 (d, *J* = 7.9 Hz, 12H), 4.43–4.27 (m, 12H), 4.10 (s, 9H), and 3.77 (s, 18H) ppm. ^{13}C NMR (100 MHz, CB-d_5) δ: 156.27, 147.66, 141.11, 141.03, 139.21, 139.04, 137.76, 137.62, 127.14, 126.75, 124.04, 121.07, 118.08, 117.71, 115.55, 114.95, 113.16, 106.98, 64.71, 64.32, 55.01, and 37.89 ppm. HR-MS *m/z* [M]$^+$ calcd for C$_{117}$H$_{90}$N$_6$O$_{12}$S$_3$, 1866.5779; found, 1867.5773. ATR-FTIR (film) v_{max}: 2928, 1602, 1500, 1436, 1359, 1332, 1277, 1237, 1172, 1085, 1034, 961, 915, 826, 759, and 726 cm^{-1}. Anal. calcd for C$_{117}$H$_{90}$N$_6$O$_{12}$S$_3$: C 75.22%, H 4.86%, N 4.50%; found: C 75.26%, H 4.82%, N 4.55%.

1.3.2   5,12,19-Trimethyl-12,19-dihydro-5*H*-benzo[*i*]benzo[6,7]indolo[3,2-*a*]benzo[6,7]indolo[3,2-*c*]carbazole (TBTAT-B-C1)

A solution of 12,19-dihydro-5*H*-benzo[*i*]benzo[6,7]indolo[3,2-*a*]benzo[6,7]indolo[3,2-*c*]carbazole (9.9 g, 20 mmol) was prepared in a mixed solvent of *N,N*-dimethylformamide and THF (*v/v*: 1/1, 500 mL) at 0 °C. To this solution, NaH (2.2 g, 90 mmol) and iodomethane (12.8 g, 90 mmol) were added sequentially while maintaining the low temperature. Subsequently, the reaction mixture was stirred at room temperature for 3 hours. To quench the reaction, 10 mL of water was slowly introduced. Removal of the organic solvent was carried out under vacuum, followed by the addition of an extra 100 mL of water. The resulting suspension was subjected to sonication, filtration, and subsequent drying, yielding the white product TBTAT-B-C1 (10.5 g) in a 98% yield. Meltling point: > 300 °C. ^{1}H NMR (400 MHz, THF-d_8) δ: 8.86 (d, J = 8.4 Hz, 3H), 8.77 (d, J = 8.6 Hz, 3H), 8.10 (d, J = 7.9 Hz, 3H), 7.88 (d, J = 8.7 Hz, 3H), 7.69 (t, J = 7.2 Hz, 3H), 7.54 (t, J = 7.2 Hz, 3H), and 4.80 (s, 9H) ppm. Due to the limited solubility of TBTAT-B-C1, a reliable ^{13}C NMR spectrum could not be obtained. HR-MS *m/z* [M]$^+$ calcd for $C_{39}H_{27}N_3$, 537.2205; found, 537.2200. ATR-FTIR (film) v_{max}: 3044, 2957, 2927, 1576, 1457, 1393, 1365, 1303, 1280, 1132, 1064, 796, 734, and 675 cm^{-1}. Anal. calcd for $C_{39}H_{27}N_3$: C 87.12%, H 5.06%, N 7.82%; found: C 87.15%, H 5.10%, N 7.79%.

1.3.3   7,14,21-Tribromo-5,12,19-trimethyl-12,19-dihydro-5*H*-benzo[*i*]benzo[6,7]indolo[3,2-*a*]benzo[6,7]indolo[3,2-*c*]carbazole (1)

A solution of TBTAT-B-C1 (1 g, 1.9 mmol) was prepared by dissolving it in dichloromethane (1 L), followed by the gradual addition of liquid bromine (0.9 g, 5.7 mmol) at a temperature of −40 °C. The reaction mixture was stirred for a duration of 8 hours at ambient temperature. The reaction was quenched by introducing a diluted solution of sodium sulfite (50 mL). The resultant organic layer was subjected to water washing and then dried over anhydrous sodium sulfate. Removal of the solvent under vacuum resulted in the formation of the purple product 1 (2.7 g), with an impressive yield of 98%. Meltling point: > 300 °C. Due to the limited solubility of compound 1, reliable ^{1}H NMR and ^{13}C NMR spectra could not be obtained. HR-MS *m/z* [M]$^+$ calcd for $C_{39}H_{24}Br_3N_3$, 772.9500; found, 772.9507. ATR-FTIR (film) v_{max}: 2921, 1594, 1455, 1352, 1194, 1074, 920, 859, 736, and 687 cm^{-1}. Anal. calcd for $C_{39}H_{24}Br_3N_3$: C 60.49%, H 3.12%, N 5.43%; found: C 60.52%, H 3.10%, N 5.49%.

1.3.4   4,4',4''-((5,12,19-Trimethyl-12,19-dihydro-5*H*-benzo[*i*]benzo[6,7]indolo[3,2-*a*]benzo[6,7]indolo[3,2-*c*]carbazole-7,14,21-triyl)tris(2,3-dihydrothieno[3,4-*b*][1,4]dioxine-7,5-diyl))tris(*N,N*-bis(4-methoxyphenyl)aniline) (TBTAT-B-C1-e3)

With compound 1 as the starting material, TBTAT-B-C1-e3 was prepared using the similar protocol for TBTAT-A-C1-e3 in 82% yield. Melting point: > 300 °C. ^{1}H NMR (400 MHz, THF-d_8) δ: 8.95 – 8.81 (m, 6H),

8.33 (d, J = 8.3 Hz, 3H), 7.74 – 7.60 (m, 9H), 7.53 (t, J = 7.6 Hz, 3H), 7.05 (t, J = 6.1 Hz, 12H), 6.94 (d, J = 8.8 Hz, 6H), 6.85 (d, J = 9.0 Hz, 12H), 4.79 (s, 9H), 4.42–4.26 (m, 12H), and 3.76 (s, 18H) ppm. ^{13}C NMR (100 MHz, THF-d_8) δ: 157.34, 148.35, 141.98, 140.97, 140.19, 139.87, 138.55, 131.54, 128.79, 127.64, 127.40, 127.02, 126.11, 125.76, 125.18, 124.14, 121.65, 120.47, 117.60, 115.61, 114.16, 106.65, 65.95, 65.56, 55.76, and 43.01 ppm. HR-MS m/z [M]$^+$ calcd for $C_{117}H_{90}N_6O_{12}S_3$, 1867.5812; found, 1867.5805. ATR-FTIR (film) v_{max}: 2928, 1602, 1500, 1436, 1359, 1332, 1277, 1237, 1172, 1085, 1034, 961, 915, 826, 759, and 726 cm^{-1}. Anal. calcd for $C_{117}H_{90}N_6O_{12}S_3$: C 75.22%, H 4.86%, N 4.50%; found: C 75.20%, H 4.89%, N 4.52%.

1.4 Crystallographic analysis

Single crystals of TBTAT-A-C1, TBTAT-B-C1, and TBTAT-A-C6 were grown from a nearly saturated solution comprising dichloromethane and heptane at 4 °C, employing a gradual solvent evaporation technique. X-ray diffraction analyses of resulting single crystals were conducted using a D8 Venture diffractometer (Bruker). Crystallographic characterization of the single crystal structures was accomplished utilizing the SHELXTL software. Comprehensive refinement parameters can be found in the accompanying single crystal .cif file. For enhanced accessibility and reference, the crystallographic data for TBTAT-A-C1, TBTAT-B-C1, and TBTAT-A-C6 have been deposited as supplementary publication numbers 2287236, 2287234, and 2287235, respectively, at the Cambridge Crystallographic Data Center.

1.5 Thin film conductivity

The deposition of an organic semiconductor layer onto interdigital gold electrodes was achieved via spin-coating a chlorobenzene solution at 2,500 rpm. The solution formulations consisted of 50 mg mL^{-1} of the organic semiconductor, 132 mM of TBP, and TBPHTFSI at concentrations of 0, 2.6, 5.6, and 8.8 mg mL^{-1}. The interdigital electrodes, fabricated on SiO$_2$, were comprised of 119 channels, each characterized by a channel length (L) of 1.5 mm, a channel width (W) of 10 μm, and a channel thickness (t) of 110 nm. After preparation, the device underwent storage under controlled dry air conditions (with relative humidity < 5%) for a period of 7 days before measurement. The direct-current electrical conductivity (σ) of the organic semiconductor thin film, in contact with the interdigital gold electrodes, was extracted from the current–voltage (I–V) curve over a bias potential range of −1.5 V to 1.5 V. The I–V curve was captured using a Keithley 2400 source meter. The σ value was determined employing the equation: $\sigma = sW / (119Lt)$. In this context, 's' corresponds to the slope derived from the linear fitting of the I–V plot. Notably, it was observed that the σ value of the organic semiconductor layer attained a stable state after approximately 5 days of storage in dry air, and thereafter remained unchanging. This observation implies that the air doping process had reached a state of equilibrium.

1.6 Hole density

In order to quantify the hole density (p) within the organic semiconductor layer exclusively composed of an organic semiconductor, we employed a metal-insulator-semiconductor (MIS) device architecture. The MIS device, denoted as n^{++}-Si/SiO$_2$/p-BCB/organic semiconductor/Au, comprises a heavily n-type doped Si substrate with a 300-nm-thick SiO$_2$ insulating layer. The smooth polybenzocyclobutene (p-BCB) organic insulating layer was formed by annealing a BCB layer at 250 °C for 1 hour. Deposition of the BCB layer was accomplished through a spin-coating procedure utilizing a 1 mg mL^{-1} BCB solution in chlorobenzene. Subsequently, the organic semiconductor layer was spin-coated onto the p-BCB layer, followed by vacuum deposition of a gold electrode. For impedance spectrum acquisition of the MIS device under a bias potential (V), the AutolabPGSTAT302N electrochemical workstation was employed. Determination of capacitance (C) utilized the equation: $C = -\dfrac{1}{\omega}[\dfrac{Z'' - \omega L_i}{(Z' - R_s)^2 + (Z'' - \omega L_i)^2}]$, where Z' and Z'' correspond to the real and imaginary components of the impedance spectrum, respectively. R_s denotes the series resistance, L_i signifies the parasitic inductance, and ω represents the angular frequency. The $C-V$ characteristic exposes the accumulation and depletion regimes of the organic semiconductor layer. Subsequently, the p can be calculated using the equation: $p = \dfrac{2}{q\varepsilon_r\varepsilon_0 \dfrac{d(A/C)^2}{dV}}$, where q denotes the elementary charge, ε_r represents the relative permittivity, ε_0 is the vacuum permittivity, and A corresponds to the area of the gold electrode.

Reliable determination of the p value within the organic semiconductor layer containing TBPHTFSI presented a formidable challenge. To surmount this, a comparative methodology relying on the quadratic integral intensities of electron paramagnetic resonance (EPR) signals from organic semiconductor layers with and without TBPHTFSI was adopted. This estimation was based on the known p value of the organic semiconductor layer devoid of TBPHTFSI, serving as a reference. Specifically, an organic semiconductor layer was spin-coated onto a 2 cm × 2 cm microslide and then stored in a dry air environment for 7 days. The resulting sample was finely crushed and loaded into a borosilicate glass tube for EPR measurements using a Bruker A300-10/12 spectrometer. By comparing EPR signals of the organic semiconductor layer with and without TBPHTFSI, an estimation of p in the presence of TBPHTFSI was obtained.

1.7 Fabrication of perovskite solar cell

The SnO$_2$ electron transport layer,[5] the FAPbI$_3$ perovskite layer,[6] and the melamine resin interlayer[7] were deposited in accordance with established procedures found in prior literature. A comprehensive description of the

perovskite solar cell preparation process is provided below. A laser-etched indium tin oxide (ITO) glass substrate with a sheet resistance of 12 Ω sq^{-1} and a thickness of 1.6 mm underwent a meticulous cleaning regimen. It was successively rinsed with detergent, deionized water, acetone, and isopropanol (IPA), each for a duration of 10 minutes in an ultrasonic bath. Subsequently, a thin layer of SnO_2 nanoparticles (3%, diluted in deionized water) was deposited onto the ITO glass through spin-coating at 3000 rpm for 30 seconds. The coated substrate was then annealed under ambient air conditions at 150 °C for 30 minutes. Following UV-ozone treatment, the glass/ITO/SnO_2 substrates were transferred into a glove box filled with dry air (<3% relative humidity) to facilitate the deposition of the perovskite layer. Fabrication of the perovskite layer was accomplished via a two-step spin-coating method. Initially, a solution containing 1.5 M PbI_2 and 7.5 mM RbCl within a DMF/DMSO solvent mixture (*v*/*v*, 9/1) was spin-coated onto the SnO_2 layer at 1500 rpm for 30 seconds, followed by annealing at 70 °C for 1 minute. Subsequently, upon the cooling of the PbI_2 layer to room temperature, a mixture solution of FAI/MACl (90 mg/13.5 mg in 1 mL IPA) was spin-coated onto the PbI_2 layer at 1800 rpm for 30 seconds. The resulting film was then annealed at 150 °C for 30 minutes, facilitating the formation of the $FAPbI_3$ perovskite layer that contained a slight presence of $(PbI_2)_2RbCl$ and PbI_2. An interlayer of melamine resin was subsequently deposited via spin-coating a HMMM solution (2 mg mL^{-1} in IPA) onto the perovskite layer at 3000 rpm for 30 seconds, followed by annealing at 110 °C for 30 minutes. This was followed by the deposition of a hole transport layer (HTL), achieved by employing a chlorobenzene solution containing 50 mg mL^{-1} of the organic semiconductor, 132 mM of TBP, and 8.8 mg mL^{-1} of TBPHTFSI, and spin-coated at a speed of 5000 rpm. Lastly, an 80-nm-thick gold electrode was deposited atop the HTL through thermal evaporation under a vacuum of less than 10^{-4} Pa. The resulting device with an active area of 0.26 cm^2 was laminated with a high-quality anti-reflective film on the glass side and a waterproof adhesive tape on the gold electrode side.

1.8 Photocurrent–photovoltage characteristic and external quantum efficiency

Photocurrent density–photovoltage (*J*–*V*) curves were acquired using a Keithley 2400 source meter. The measurements were automated through Labview 14.0. The incident light was generated by an LS1000-4S-AM solar simulator (Solar Light Company), delivering AM1.5G sunlight at an irradiation level of 100 mW cm^{-2} (verified by a calibrated silicon solar cell). A black metal mask with an aperture area of 0.16 cm^2 was employed to define the photoactive region. The devices were subjected to both reverse scans (1.2 V→−0.1 V, step 0.005 V) and forward scans (−0.1 V→1.2 V, step 0.005 V). External quantum efficiency (EQE) measurements utilized an Omni-λ300 monochromator (Zolix) paired with a 150 W xenon lamp (Zolix) for monochromatic light supply. Photocurrent was recorded using a Keithley 2400 source meter. A Hamamatsu S1337-1010BQ silicon diode,

calibrated at the National Institute of Metrology, was employed to measure the intensity of the monochromatic light.

1.9 Operation stability and thermostability

To achieve maximum power point (MPP) tracking of perovskite solar cells, a 16-channel photovoltaic tracking system (YH Electronic Equipment Business) was employed in conjunction with an SLS-LED-80A solar simulator (Qingdao Solar Scientific Instrument High-tech Co., LTD). This experimental setup was integrated with a nitrogen-filled glovebox to ensure controlled environmental conditions for solar cells. The MPP data were acquired at 5-minute intervals utilizing the perturb and observe method, which guarantees accurate monitoring of performance parameters at the MPP. To evaluate the thermal stability of the perovskite solar cells, they were stored in an FD56 oven (Binder) set at 85 °C. The ambient humidity surrounding the oven ranged between 40% and 95%. Intermittent J–V measurements were conducted under AM1.5G conditions at the room temperature.

1.10 Morphology

Polarization optical microscope (POM) images were acquired using the SDPTOP CX40P system from Sunny Optical Technology. Scanning electron microscope (SEM) images were obtained through the use of an SU8010 microscope provided by Hitachi. Fluorescence optical microscope (FOM) images were captured employing the ECLIPSE Ti-U system by Nikon. Atomic force microscopy (AFM) measurements were conducted using the Park NX10 microscope from Park Systems. AFM-IR images were collected using the nanoIR2-FS system from Anasys Instruments, utilizing gold-coated probes and enhancing resonance via a pulsed quantum cascade laser.

2 Theoretical modeling

2.1 Frontier molecular orbitals

The frontier molecular orbitals energy levels were calculated employing the Gaussian 16 program suite within the framework of density functional theory (DFT) at the B3LYP/6-311G(d,p) level.

2.2 Hole transport in amorphous organic solid

In amorphous organic semiconductor, hole transport is frequently elucidated through the hopping mechanism. The rate of hopping (ω_{ij}) hinges on several pivotal factors, including the transfer integral (v_{ij}) between the hopping sites i and j, the HOMO energy discrepancy (ΔE_{ij}) between these sites, and the reorganization energy (λ) linked to hole transfer. Initially, we computed λ using the DFT approach at the B3LYP/6-311G(d,p) level. Subsequently, the construction of a cubic box with periodic boundaries was accomplished using the Amorphous Cell module within Materials Studio 8.0, encompassing 360 molecules of the molecular semiconductor. To capture the

microstructure of the amorphous assembly, molecular dynamics simulations were executed employing the COMPASS II force field. From this assembly, we generated neighbor lists, each containing a molecular pair fulfilling the criterion of having a nearest atom-to-atom distance of ≤ 5 Å. Additionally, we extracted the centroid distance (d) for each neighbor list. To assess electrostatic and polarization contributions to ΔE_{ij}, we employed the Thole model, while partial charges of molecules in both their neutral and cationic states were computed using DFT calculations at the CAM-B3LYP/6-311G(d,p) level. To evaluate energetic disorder, we adopted the Gaussian disorder model, involving the fitting of the ΔE_{ij} profile. For the computation of v_{ij}, we employed an approximate method based on ZINDO for each neighbor list. Finally, to gain insight into hole mobility, stochastic kinetic Monte Carlo simulations were performed using the VOTCA toolkit,[8] providing a comprehensive understanding of transport dynamics within the system.

2.3 Glass transition temperature, diffusivity, and permeability

We utilized the Amorphous Cell module within Materials Studio 8.0 to construct a cubic box characterized by periodic boundaries. This box comprised either 360 molecules of organic semiconductor or 360 molecules of organic semiconductor, supplemented by additional molecules of TBPHTFSI, where the weight percentage of TBPHTFSI was 15%. In order to discern the properties of these systems, we employed molecular dynamics simulations conducted with the COMPASS II force field. Additionally, the FORCITE module in Materials Studio 8.0 was harnessed to explore key properties such as the glass transition temperature (T_g) and diffusivity (D). Our simulation protocol encompassed an initial NVT simulation at 700 K utilizing a Nose thermostat, succeeded by an NPT simulation at the same temperature employing both a Nose thermostat and a Berendsen barostat. Subsequent to this, a gradual cooling process was executed, transitioning from 700 K to 200 K, while conducting NVT and NPT simulations at each temperature stage. The equilibrated specific volumes (SV) were recorded at these diverse temperatures. The theoretical T_g, designated as T_g^{SV}, was deduced by identifying the intersection of linear fitting lines in the low and high temperature regimes. To evaluate the diffusion of H_2O, TBPHTFSI, or FAI molecules in the OSC-TBPHTFSI composite, we introduced them into the system and performed NVT and NPT simulations. Trajectories were captured, and mean square displacements were analyzed to derive theoretical D values. Moreover, employing the Sorption module in Materials Studio 8.0, we conducted a grand canonical Monte Carlo simulation, specifically targeting the adsorption isotherm, to ascertain the solubilities (S) of water. Finally, the water permeabilities (P) were computed using the formula $P = D \times S$. Additionally, the FORCITE module was also employed for simulating cohesive energy density and Young's modulus.

3. References

1   L. Fang, Y. Zhang, T. Li, Y. Wei, Y. Yuan, J. Zhang and P. Wang, *Adv. Energy Mater.*, 2023, **13**, 2301455.

2   N. Xu, Y. Zhang, L. Fang, T. Li, X. Xie, J. Zhang and P. Wang, *ACS Mater. Lett.*, 2022, **4**, 11.

3   Q. Feng, X. Jia, G. Zhou, and Z.-S. Wang, *Chem. Commun.*, 2013, **49**, 7445.

4   Y. Ren, M. Ren, X. Xie, J. Wang, Y. Cai, Y. Yuan, J. Zhang and P. Wang, *Nano Energy*, 2021, **81**, 105655.

5   Q. Jiang, Y. Zhao, X. Zhang, X. Yang, Y. Chen, Z. Chu, Q. Ye, X. Li, Z. Yin and J. You, *Nat. Photon.*, 2019, **13**, 460.

6   Y. Zhao, F. Ma, Z. Qu, S. Yu, T. Shen, H.-X. Deng, X. Chu, X. Peng, Y. Yuan, X. Zhang and J. You, *Science*, 2022, **377**, 531.

7   T. Li, Y. Zhang, L. Fang, B. Zhang, Y. Yuan, J. Zhang and P. Wang, *J. Mater. Chem. A*, 2023, **11**, 15269.

8   V. Rühle, A. Lukyanov, F. May, M. Schrader, T. Vehoff, J. Kirkpatrick, B. Baumeier and D. Andrienko, *J. Chem. Theory Comput.*, 2011, **7**, 3335.
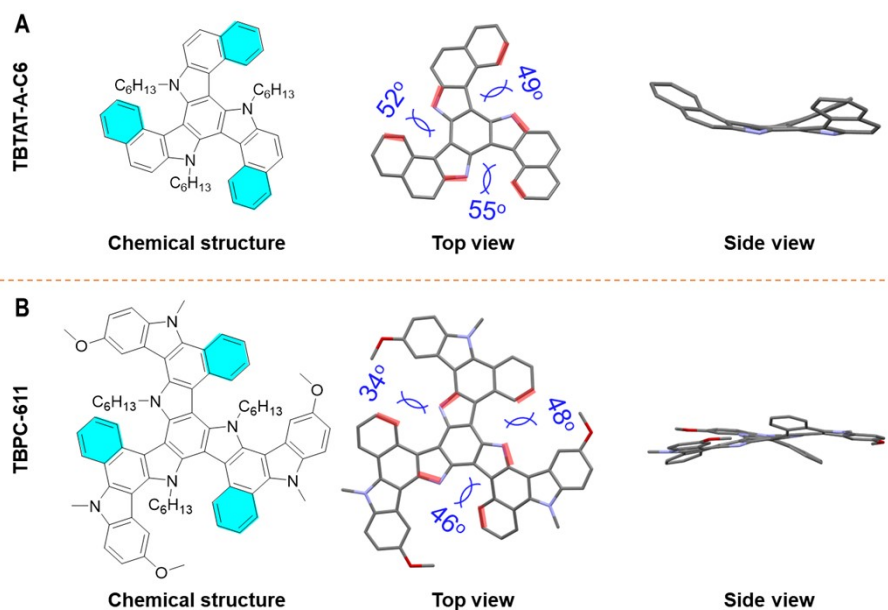
Fig. S1 (A,B) Chemical structures and crystallographic analysis of molecular geometries: (A) TBTAT-A-C6, (B) TBPC-611. Molecular geometries omit hydrogen atoms and hexyl groups for clarity. Dihedral angles are defined by the red marked chemical bonds.

Table S1. Experimental and theoretical glass transition temperature [a]

Organic semiconductor	$T_{\mathrm{g}}^{\mathrm{DSC}}$ [°C]	$T_{\mathrm{g}}^{\mathrm{SV}}$ [°C]
TBTAT-A-C1-e3	245	281
TBTAT-B-C1-e3	224	254

[a] $T_{\mathrm{g}}^{\mathrm{DSC}}$ is the experimental glass transition measured by differential scanning calorimetry. $T_{\mathrm{g}}^{\mathrm{SV}}$ is the theoretical glass transition temperature obtained by simulating the specific volume using molecular dynamics.
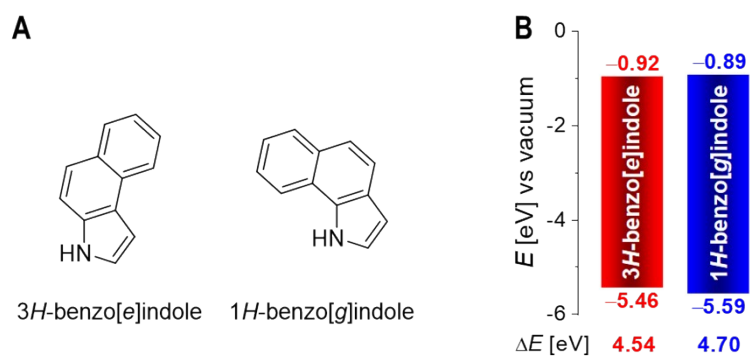
Fig. S2 (A) Chemical structures of 3*H*-benzo[*e*]indole and 1*H*-benzo[*g*]indole, which are the relevant model molecules of TBTAT-A-C1 and TBTAT-B-C1, respectively. (B) Energy diagram displaying the HOMO and LUMO energy levels, indicated below and above the color bars, respectively. The energy gap (ΔE) between HOMO and LUMO is also provided.
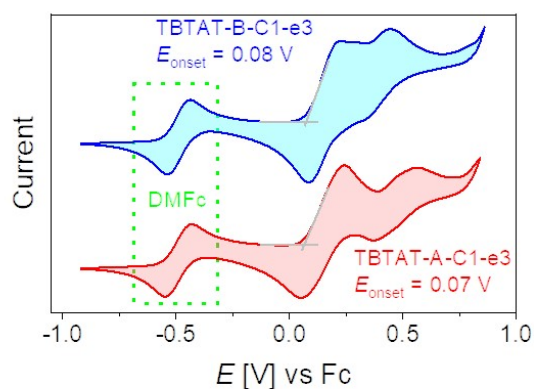
Fig. S3 Cyclic voltammograms of the organic semiconductors in tetrahydrofuran using bis(pentamethylcyclopentadienyl)iron (DMFc) as the internal reference. The potential is reported relative to ferrocene (Fc). The onset potential (E_{onset}) of the first oxidation wave is indicated.
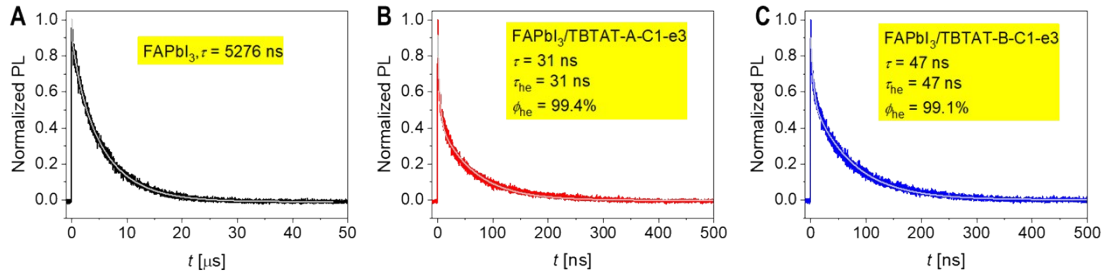
Fig. S4 TRPL curves at 805 nm for thin films of FAPbI$_3$, with and without a hole transport layer. The excitation wavelength is 670 nm. Biexponential decay fits (gray line) were conducted to yield the PL lifetimes (τ). The hole extraction yield (ϕ_{he}) can be calculated using the equation $\phi_{he} = \dfrac{\tau_1 - \tau_2}{\tau_1}$, where τ_1 denotes the amplitude-averaged lifetime of the FAPbI$_3$ thin film alone, and τ_2 represents the amplitude-averaged lifetime with a hole transport layer. The time constant of hole extraction can be calculated using the equation $\tau_{he} = \dfrac{\tau_1 \times \tau_2}{\tau_1 - \tau_2}$. The figure also presents the yield and the time constant of hole extraction.
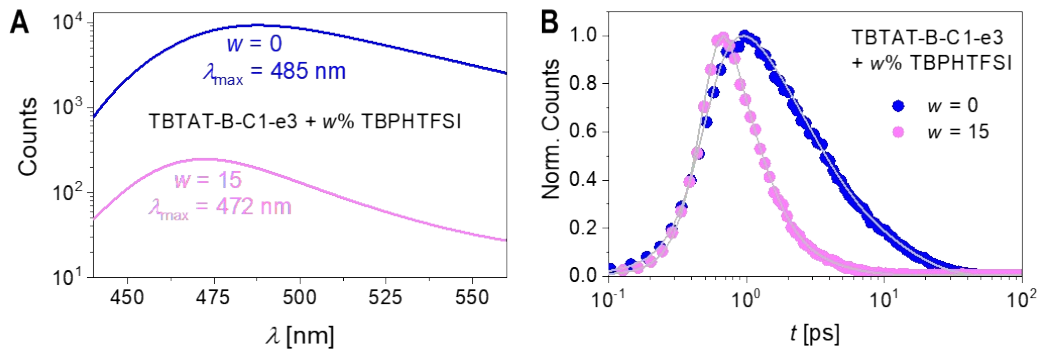
Fig. S5 (A) Static PL spectra of TBTAT-B-C1-e3 films without and with 15% TBPHTFSI. (B) Femtosecond TRPL traces of TBTAT-B-C1-e3 films without and with 15% TBPHTFSI.
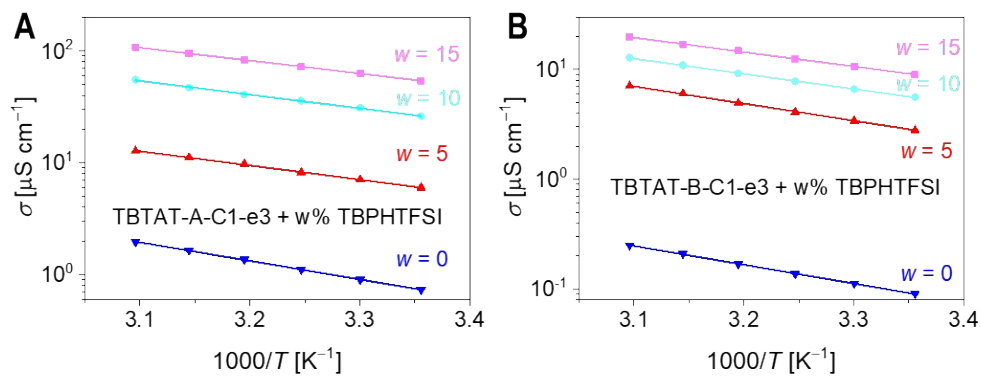
Fig. S6 Arrhenius plot of the conductivity (σ) for thin films of organic semiconductors with varying weight percentages of TBPHTFSI. *T* denotes the temperature in Kelvin.

TBTAT-A-C1-e3   **TBTAT-B-C1-e3**
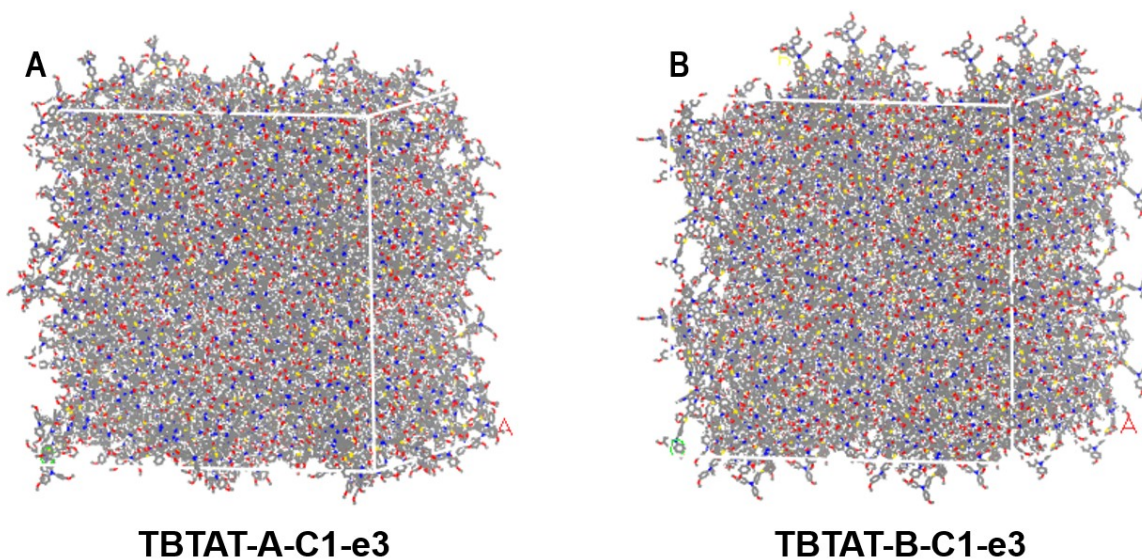
Fig. S7 Snapshots of molecular dynamics simulated amorphous systems with 360 molecules of organic semiconductor.
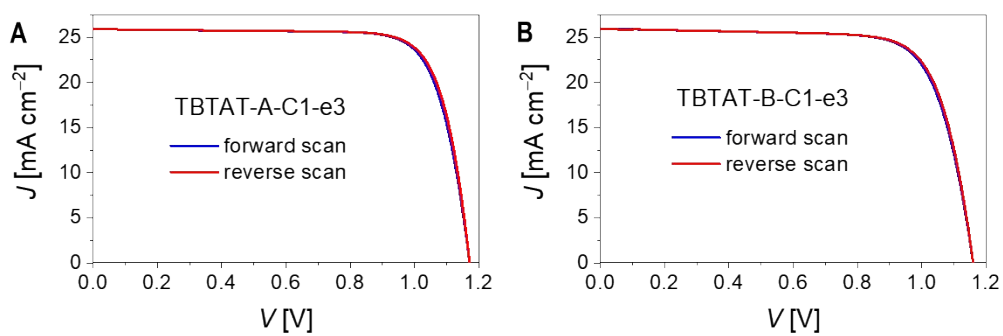
Fig. S8 Reverse and forward *J–V* curves of representative perovskite solar cells under the simulated AM1.5G irradiation. Scan rate: 50 mV s⁻¹.
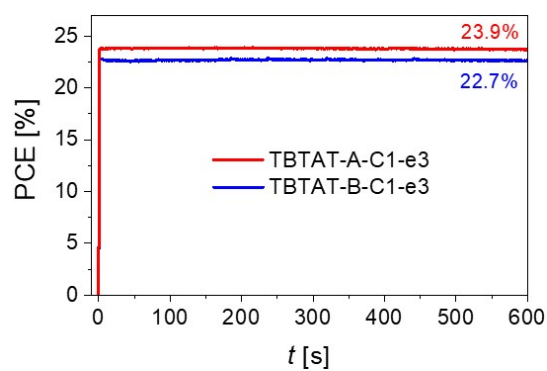
Fig. S9 Steady PCE outputs of the TBTAT-A-C1-e3 cell and the TBTAT-B-C1-e3 cell.
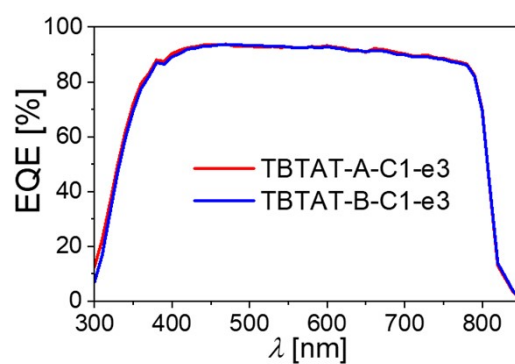
Fig. S10 EQE spectra of the unaged cells.
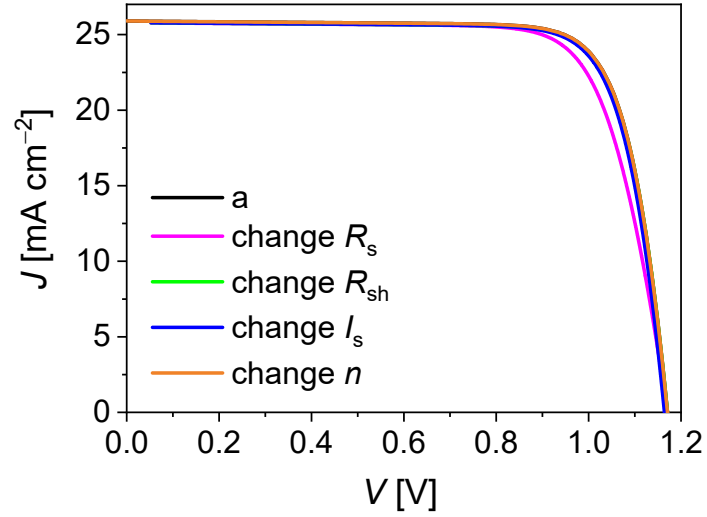
Fig. S11 Simulation of *J–V* curves using the Shockley diode equation to assess the influence of individual parameters (R_{sh} , I_s , R_s , and n) on both V_{OC} and FF . A new *J–V* curve was generated by incorporating one fitting parameter (R_{sh} , I_s , R_s , or n) from the *J–V* data of the TBTAT-B-C1-e3 cell, while retaining the remaining three fitting parameters from the *J–V* data of the TBTAT-A-C1-e3 cell. Curve a represents the *J–V* data of the TBTAT-A-C1-e3 cell and is provided for comparative purposes.

Table S2. Parameters used in $J-V$ simulation and photovoltaic parameters derived from simulated $J-V$ characteristics [a]

Replaced parameter	R_s [Ω]	R_{sh} [Ω]	I_s [pA]	n	J_{SC} [mA cm^{-2}]	V_{OC} [V]	ΔV_{OC} [V]	FF [%]	ΔFF [%]	PCE [%]
/	7	27285	1.5	2.1	25.9	1.172	/	79.0	/	23.9
R_s	**17**	27285	1.5	2.1	25.9	1.171	−0.001	75.6	−3.4	22.9
R_{sh}	7	**26868**	1.5	2.1	25.9	1.170	−0.002	78.7	−0.3	23.8
I_s	7	27285	**1.6**	2.1	25.9	1.164	−0.008	78.6	−0.4	23.7
n	7	27285	1.5	**2.1**	25.9	1.172	0	79.0	0	23.9

[a] The red marker represents the simulation parameter obtained from the measured $J-V$ data of the TBTAT-B-C1-e3 cell, while the blue markers indicate the simulation parameters derived from the measured $J-V$ data of the TBTAT-A-C1-e3 cell.
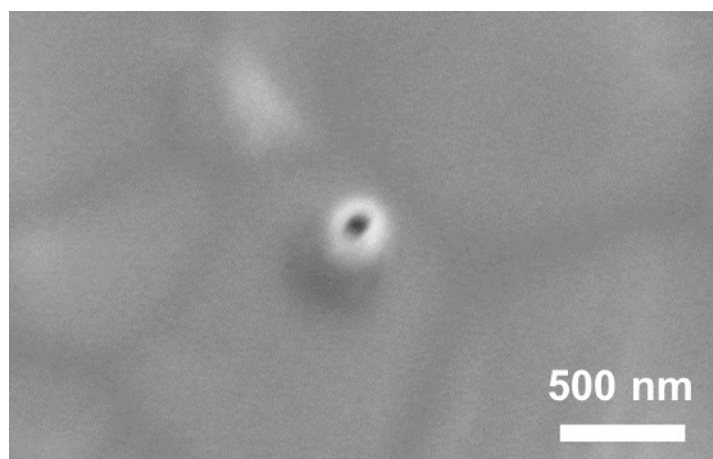
Fig. S12 Top-viewed SEM image of the pristine TBTAT-B-C1-e3 film covered on perovskite.
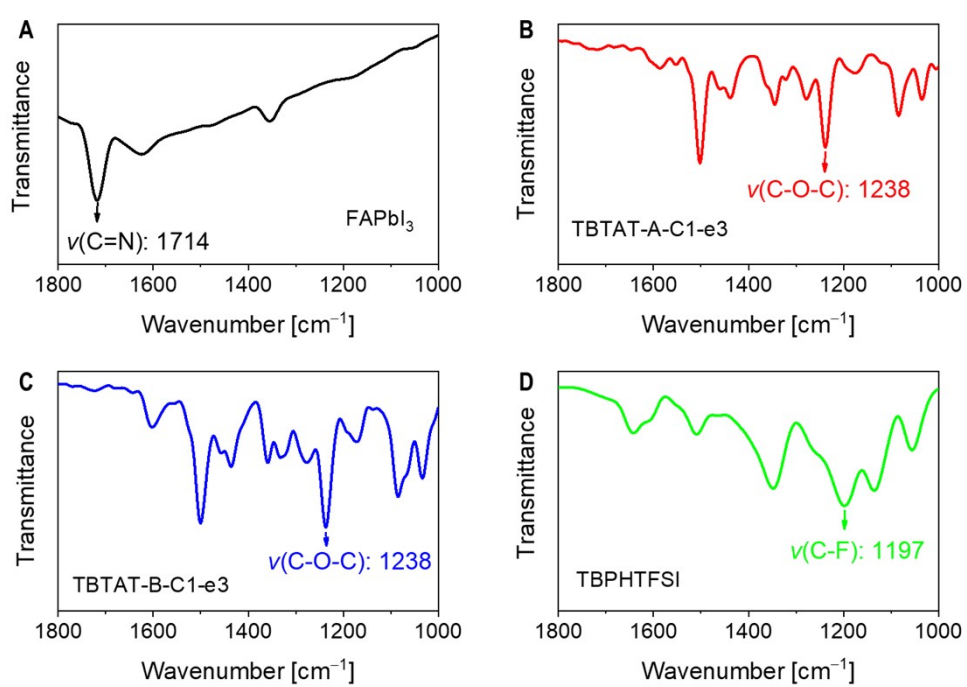
Fig. S13 ATR-FTIR spectra of thin films for (A) perovskite, (B) TBTAT-A-C1-e3, (C) TBTAT-B-C1-e3, and (D) TBPHTFSI.
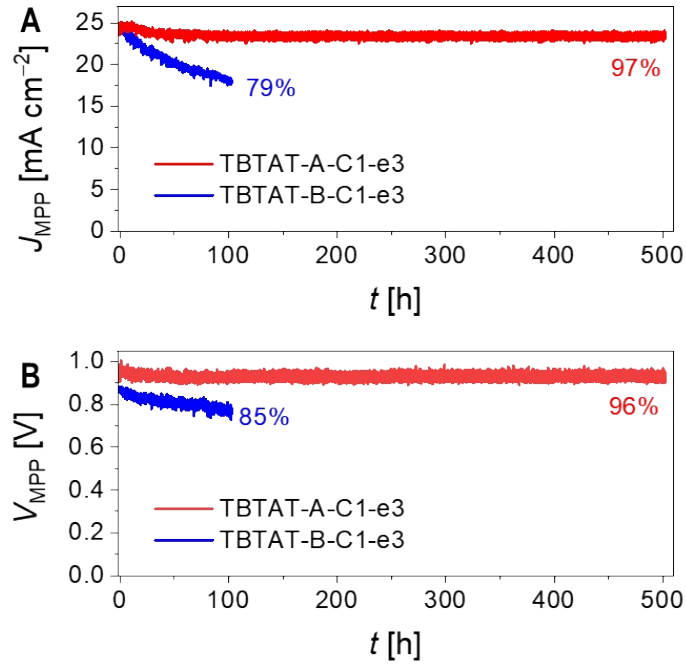
Fig. S14 Maximum power point (MPP) tracking parameters under simulated AM1.5G sunlight: (A) photocurrent density at MPP (J_{MPP}); (B) photovoltage at MPP (V_{MPP}).

	R_s [Ω]	R_{sh} [Ω]	I_s [pA]	n
TBTAT-A-C1-e3, fresh	10	24000	1.3	2.1
TBTAT-B-C1-e3, fresh	18	23050	6.2	2.2
TBTAT-A-C1-e3, aged	12	9200	47	2.4
TBTAT-B-C1-e3, aged	20	1663	278	2.2
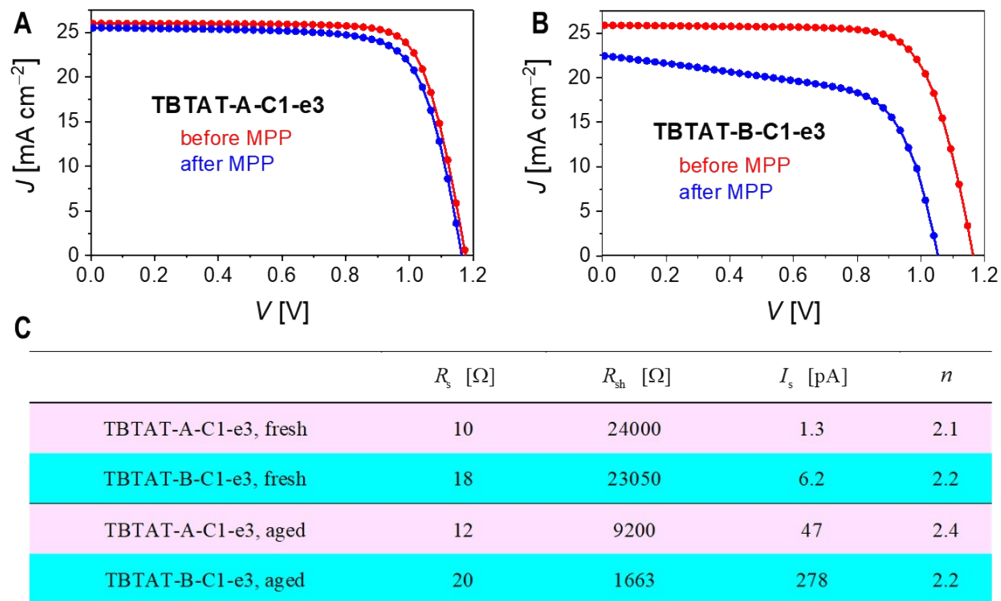
Fig. S15 (A,B) *J–V* data (dotted) before and after maximum power point (MPP) tracking. The solid lines correspond to fits based on the Schockley diode equation. (C) Parameters used in *J–V* simulation of cells before and after MPP tracking.
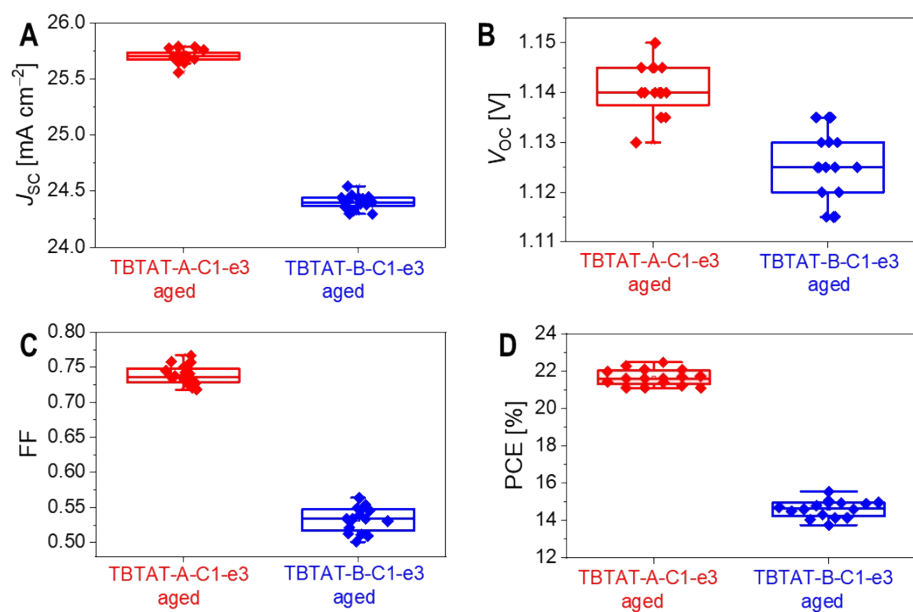
Fig. S16 (A–D) Statistical distributions of photovoltaic parameters of the aged cells: (A) J_{SC}; (B) V_{OC}; (C) FF; (D) PCE.
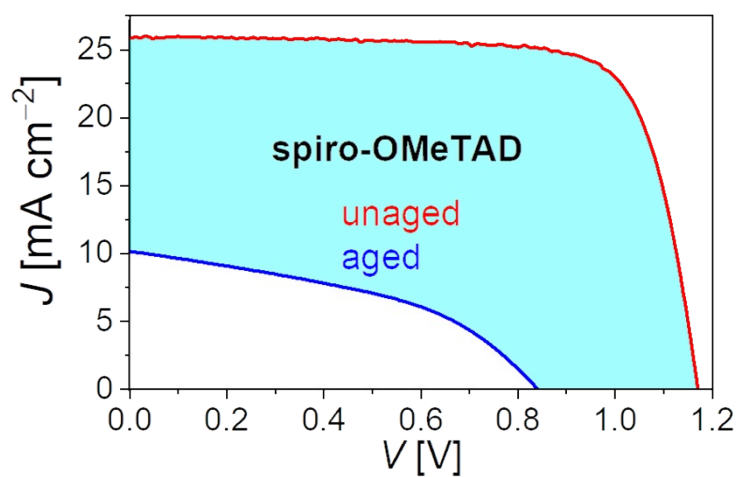
Fig. S17 Representative J–V curves under simulated AM1.5G irradiation of spiro-OMeTAD cell before and after 1000-hour, 85 °C aging.
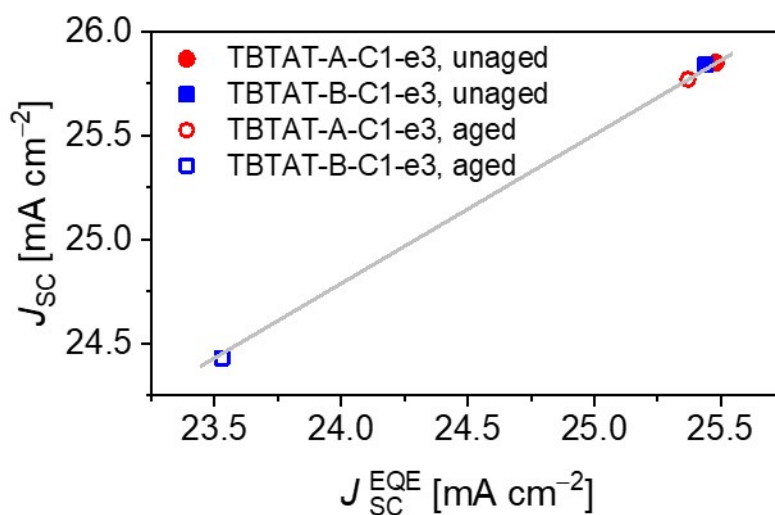
Fig S18 Correlation between J_{SC}^{EQE} and J_{sc} for the unaged and aged PSCs.

Table S3. Parameters used in $J-V$ simulation of cells before and after 85 °C aging

	R_s [Ω]	R_{sh} [Ω]	I_s [pA]	n
TBTAT-A-C1-e3, unaged	9	27263	1.4	2.1
TBTAT-B-C1-e3, unaged	22	27000	1.6	2.1
TBTAT-A-C1-e3, aged	16.4	8847	25.6	2.4
TBTAT-B-C1-e3, aged	49.3	3000	245000	4.6
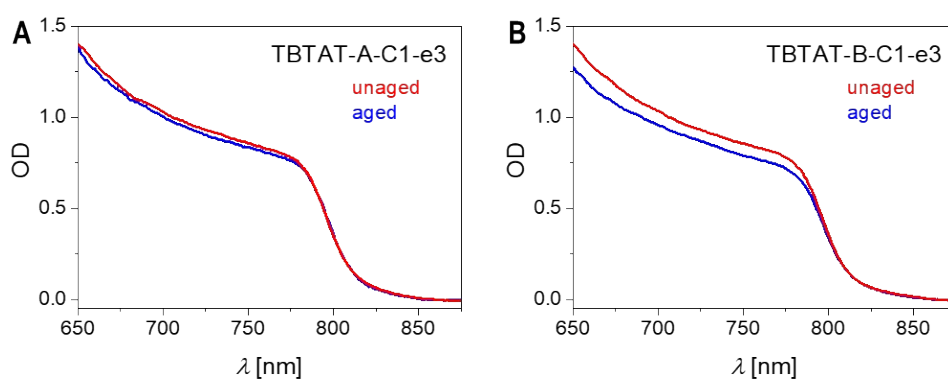
Fig. S19 (A,B) Optical densities (OD) of the unaged and aged PSCs after removal of the gold electrode.
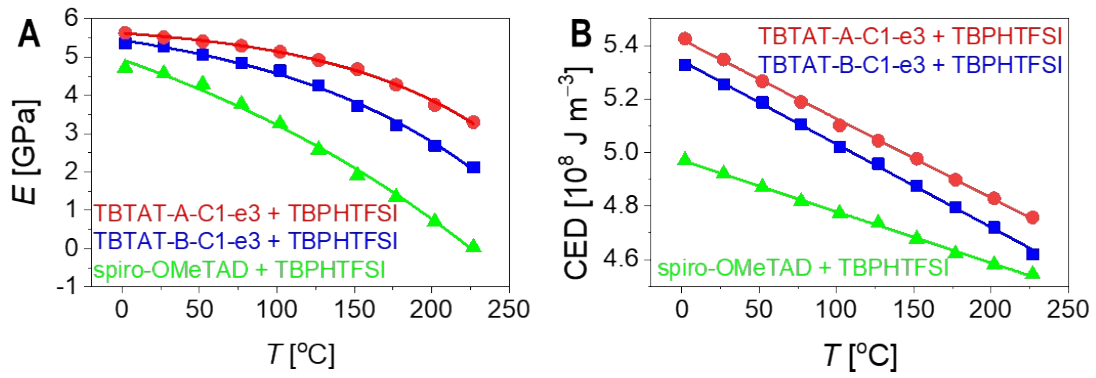
Fig. S20 (A) Temperature-dependent Young's modulus (*E*) obtained from molecular dynamic simulation. The solid line is a monoexponential fit. (B) Theoretical cohesive energy density (CED) as a function of *T*. The solid line represents a linear fit.
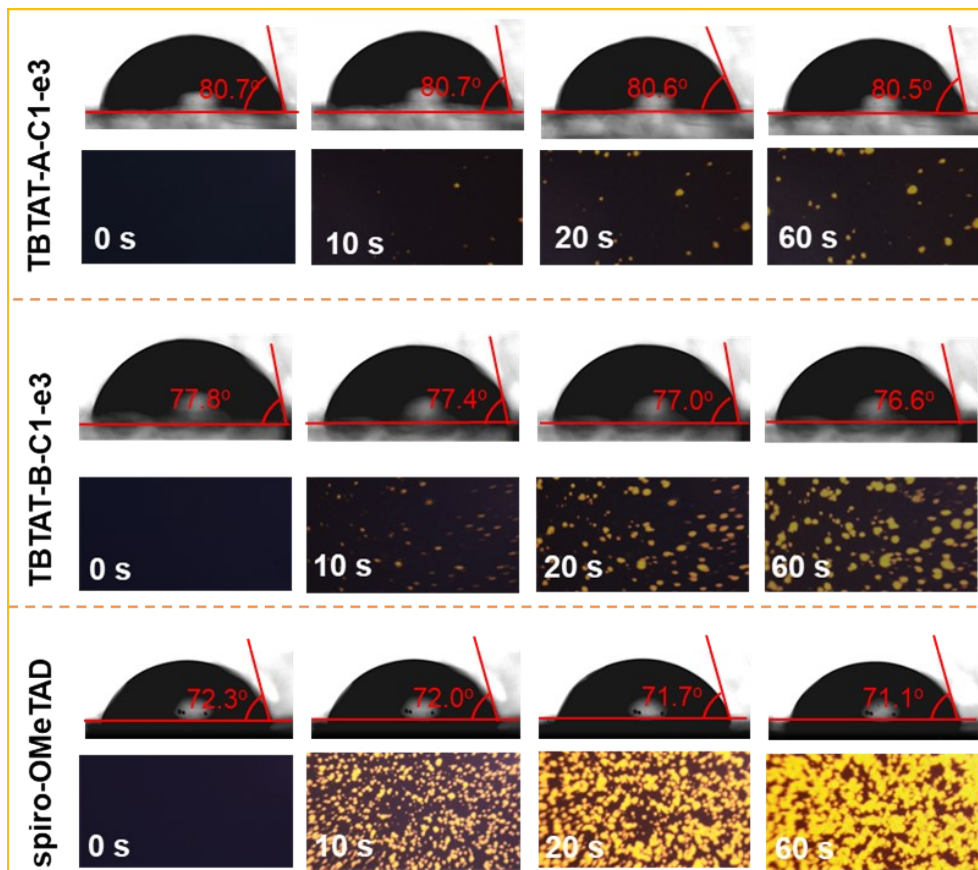
Fig. S21 Evolution of water contact angle and the POM images of a perovskite film under a water droplet over time. The size of POM images is 500 μm × 250 μm.
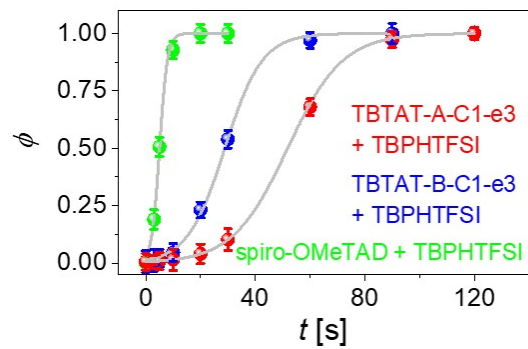
Fig. S22 (A) Plots of the fraction of the yellow region (ϕ) as a function of time (t). The solid lines refer to the Bohart-Adams fits.

5   Appendix: ¹H NMR Spectra, ¹³C NMR Spectra, HR-MS, and ATR-FTIR
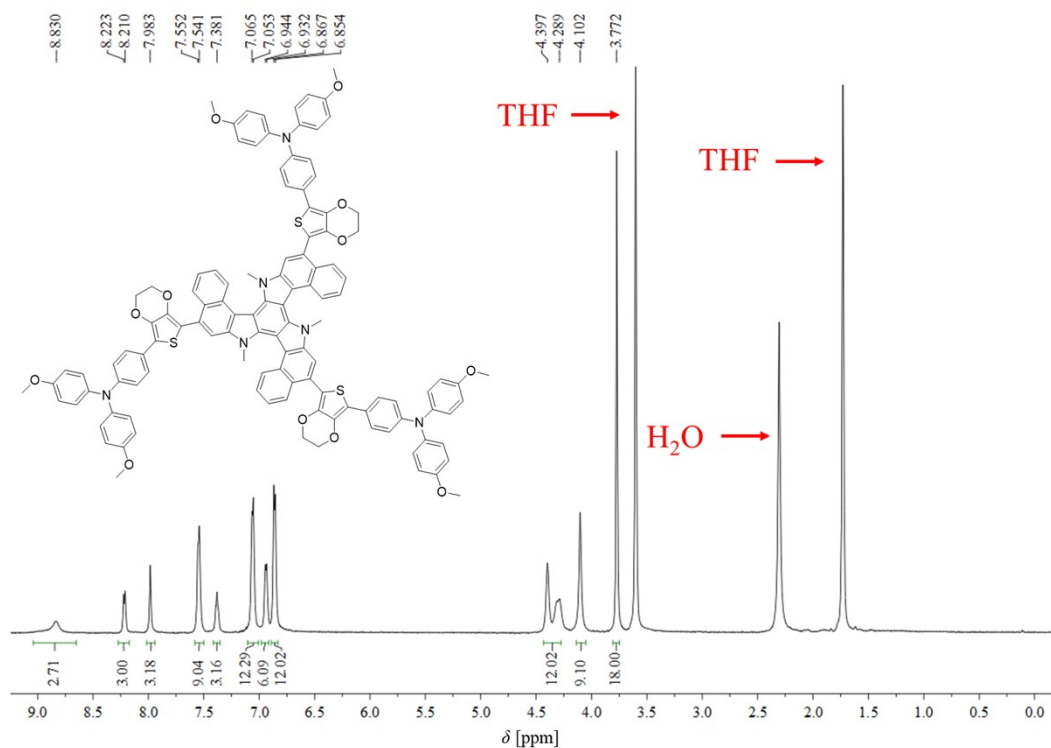
Fig. S23 ¹H NMR (600 MHz) spectrum of TBTAT-A-C1-e3 in THF-*d*₈.
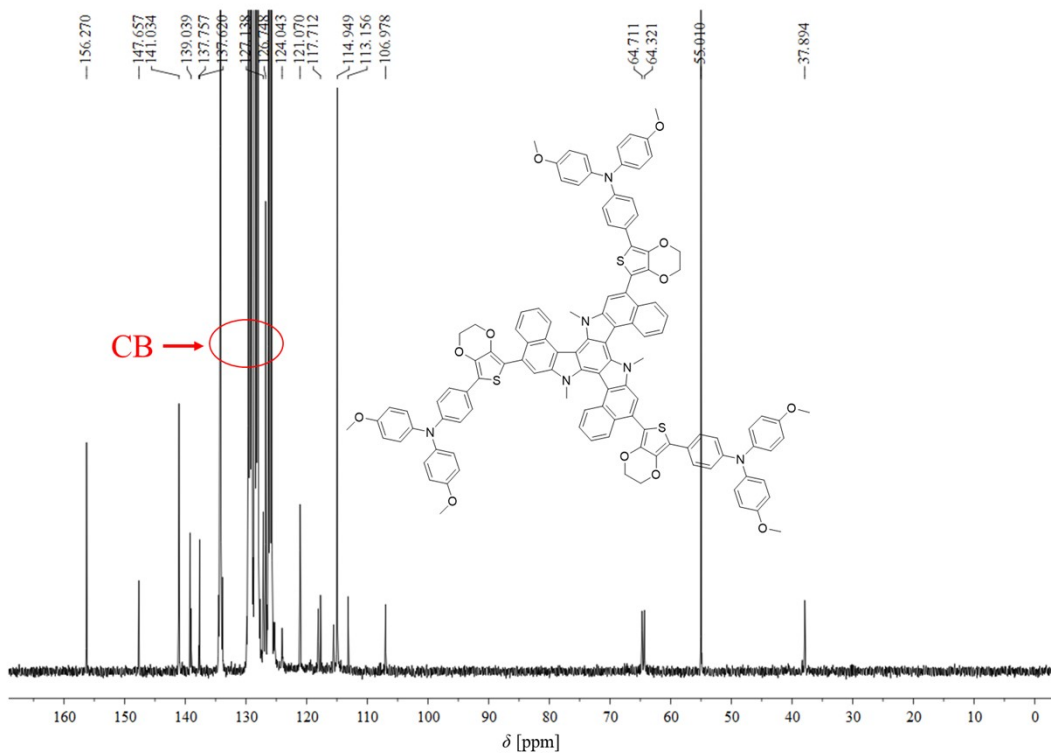
Fig. S24 ¹³C NMR (100 MHz) spectrum of TBTAT-A-C1-e3 in CB-*d*₅.
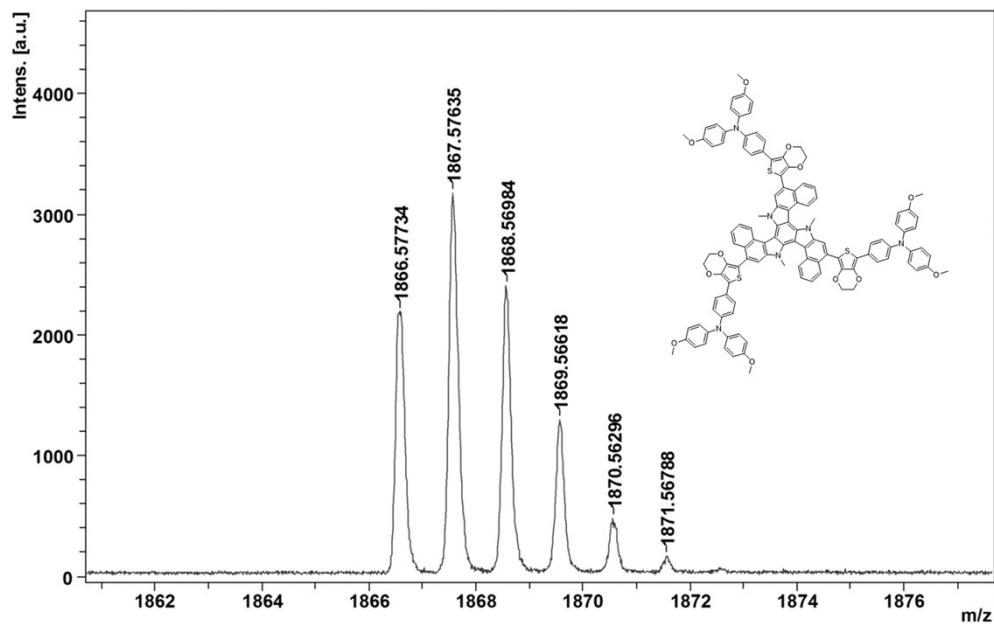
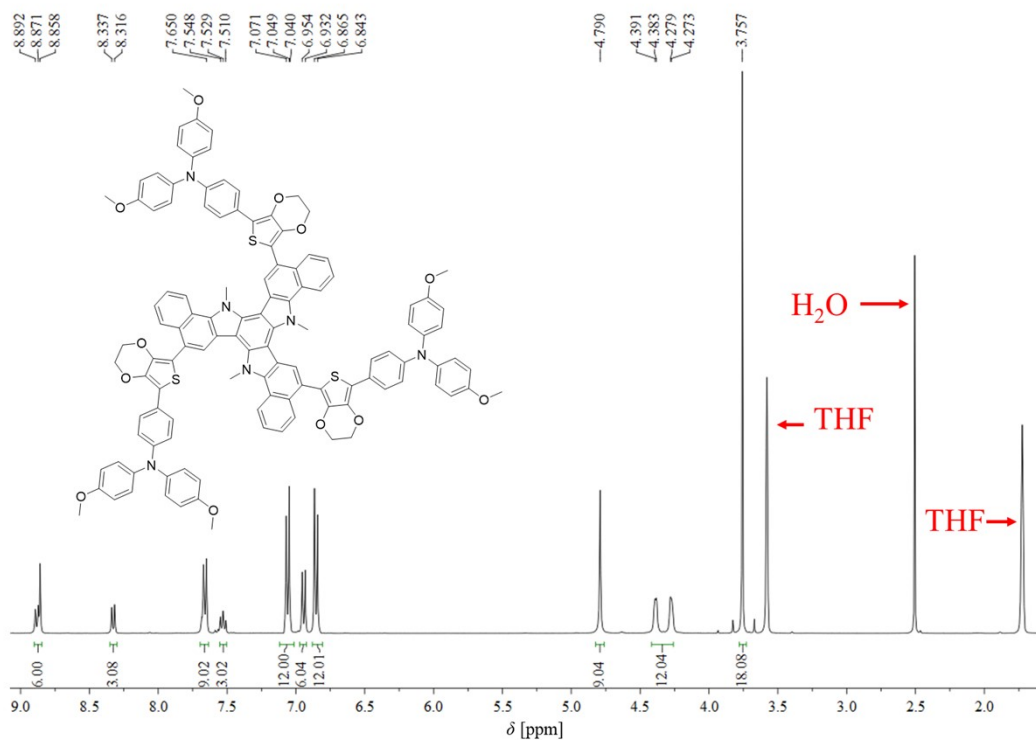**Fig. S25** HR-MS of TBTAT-A-C1-e3.
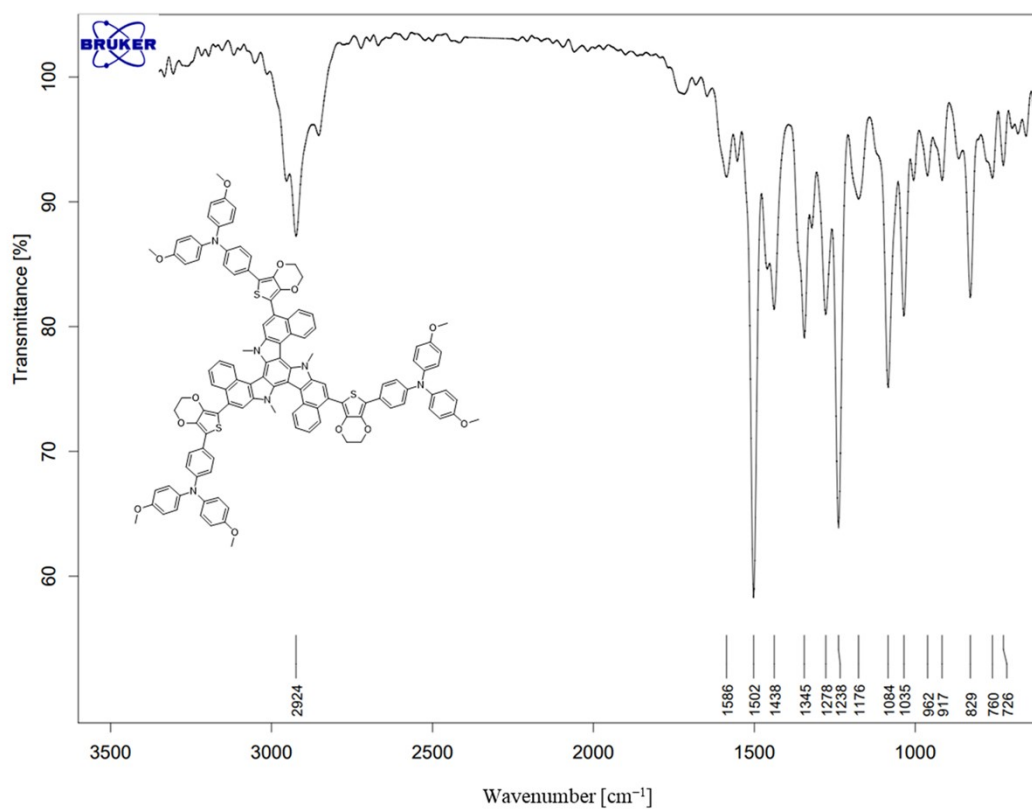
Fig. S26 ATR-FTIR of TBTAT-A-C1-e3.
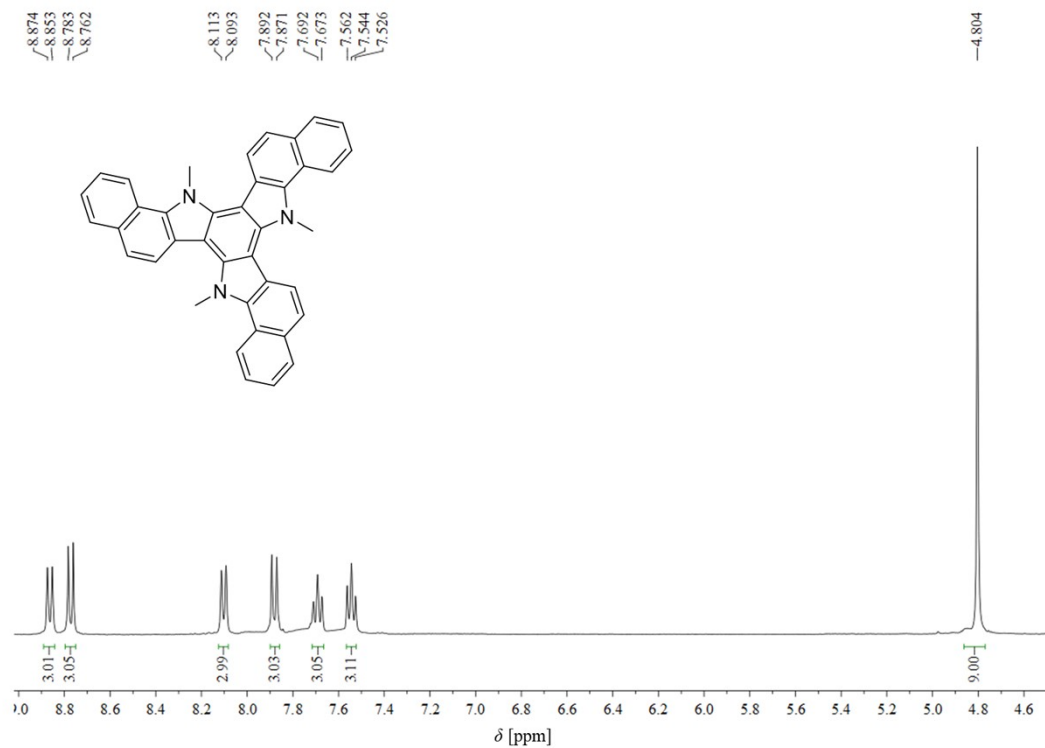
Fig. S27 ^{1}H NMR (400 MHz) spectrum of TBTAT-B-C1 in THF-d_8.
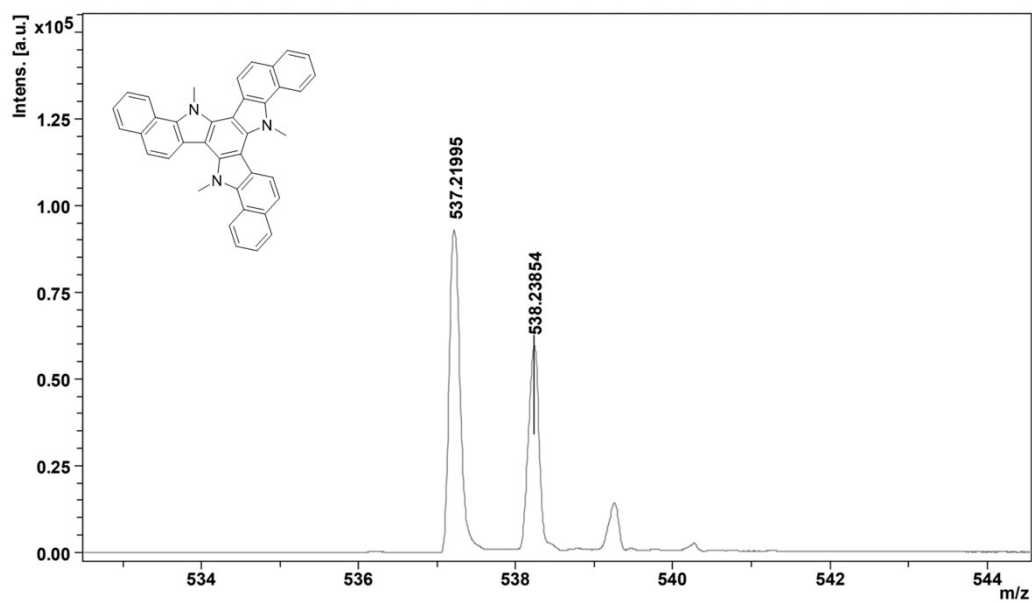
Fig. S28 HR-MS of TBTAT-B-C1.
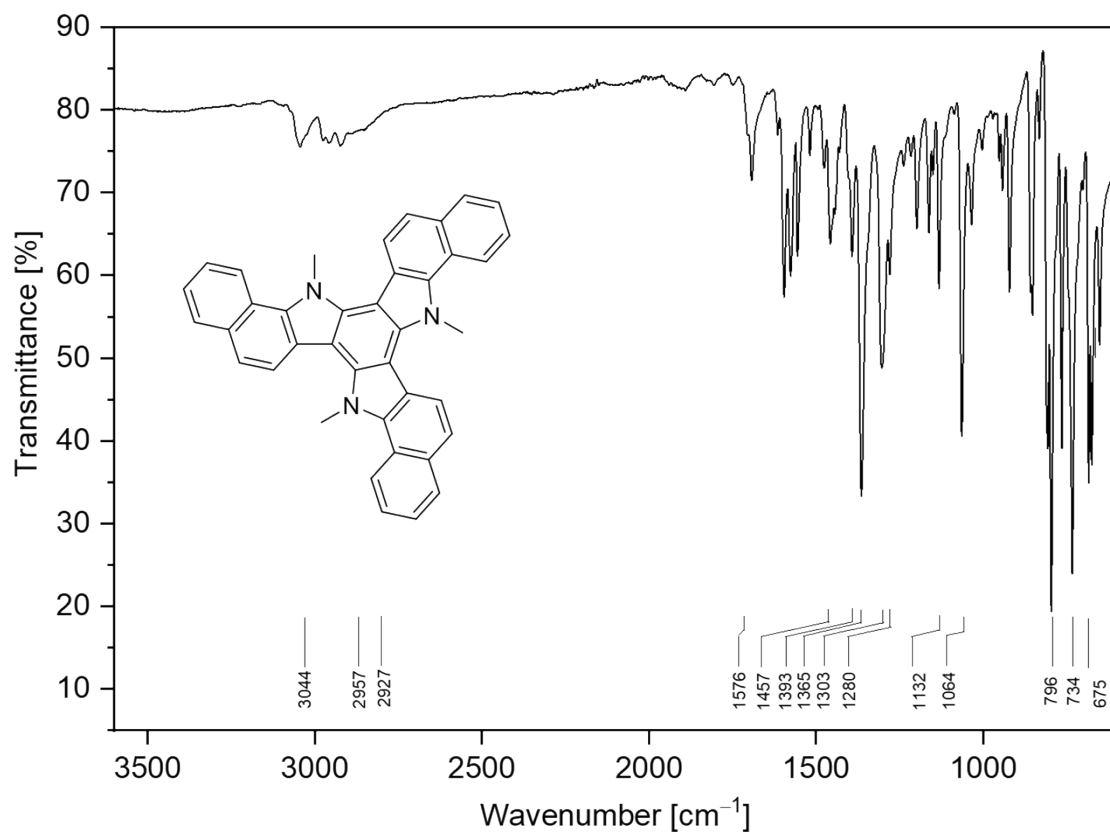
Fig. S29 ATR-FTIR of TBTAT-B-C1.
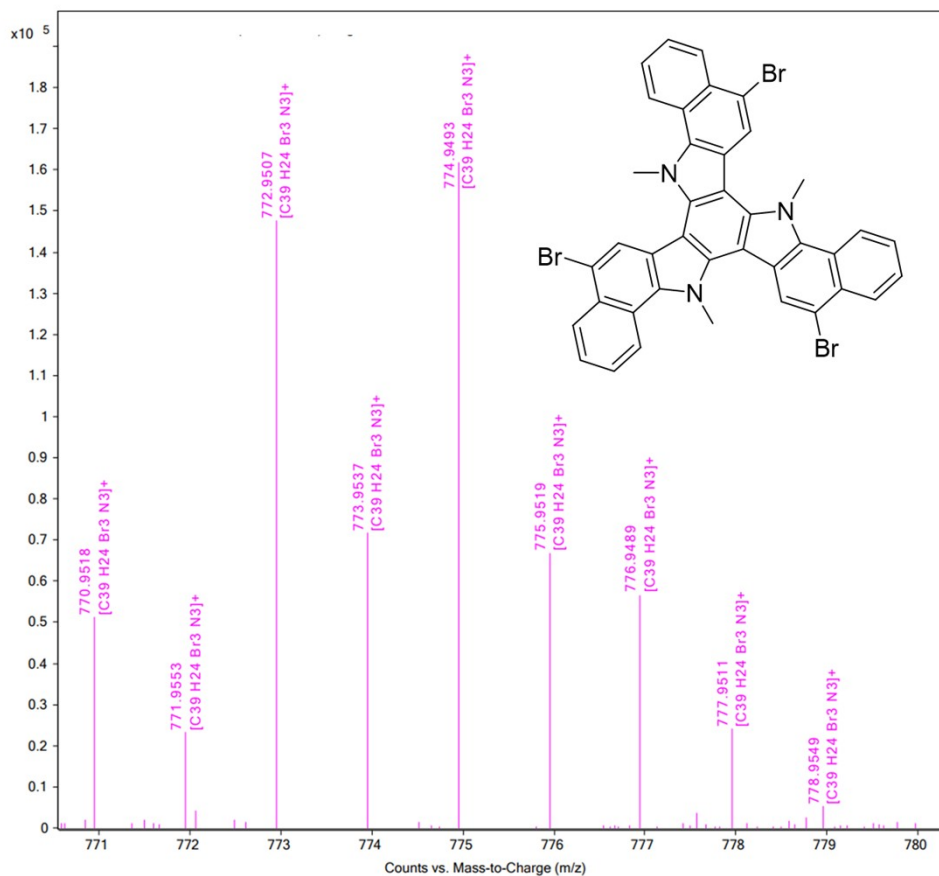
Fig. S30 HR-MS of compound 1.
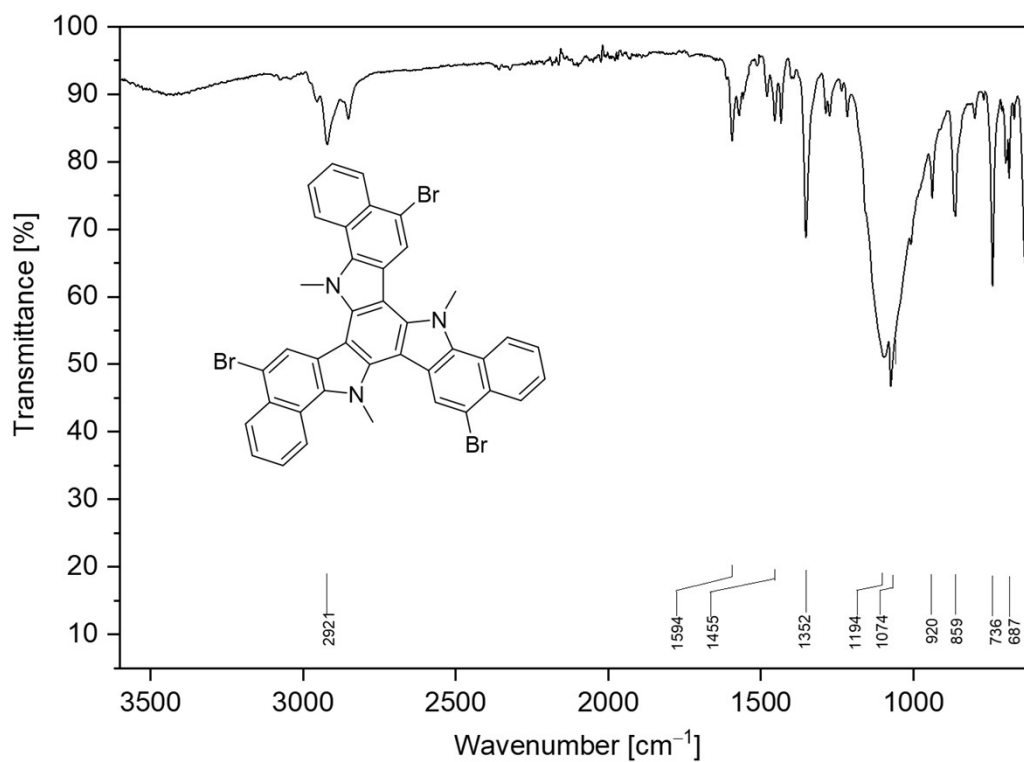
Fig. S31 ATR-FTIR of compound 1.

Fig. S32 ^{1}H NMR (400 MHz) spectrum of TBTAT-B-C1-e3 in THF-d_8.
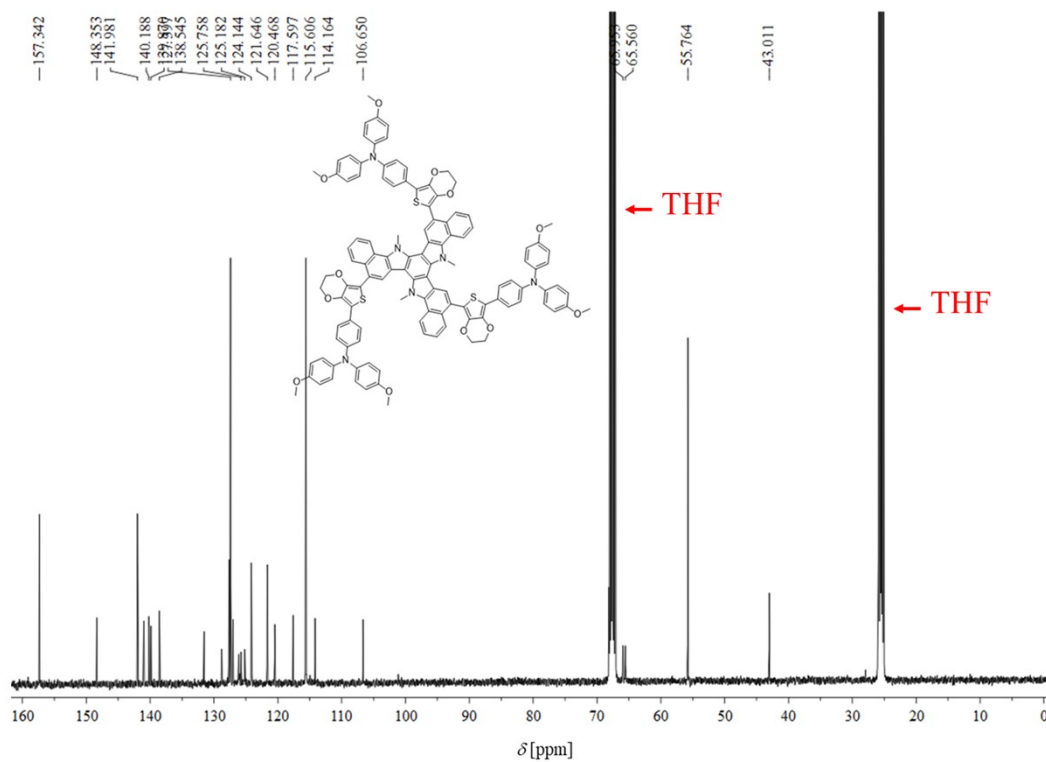

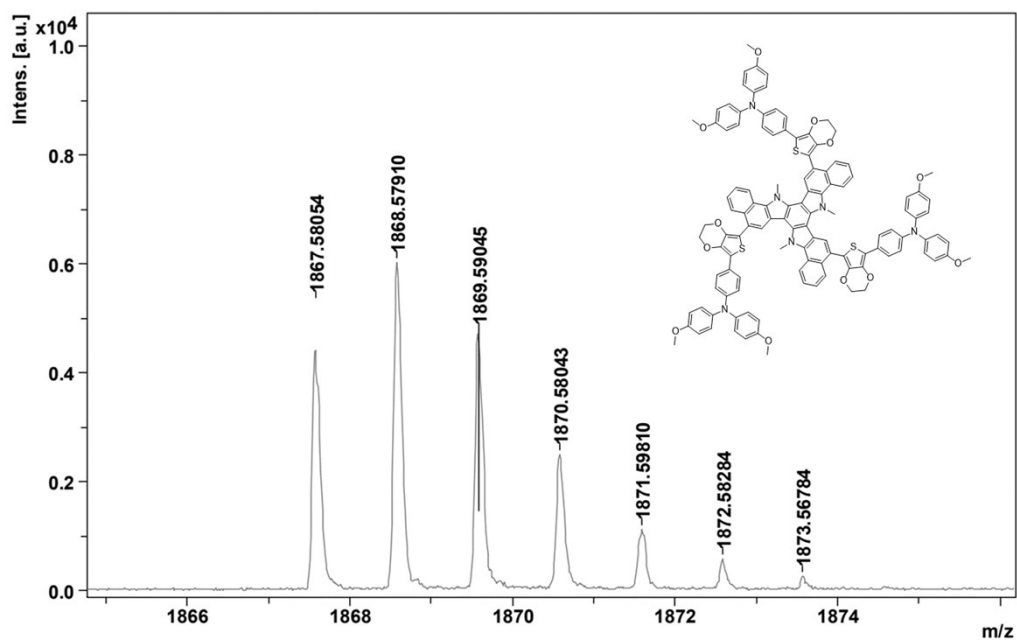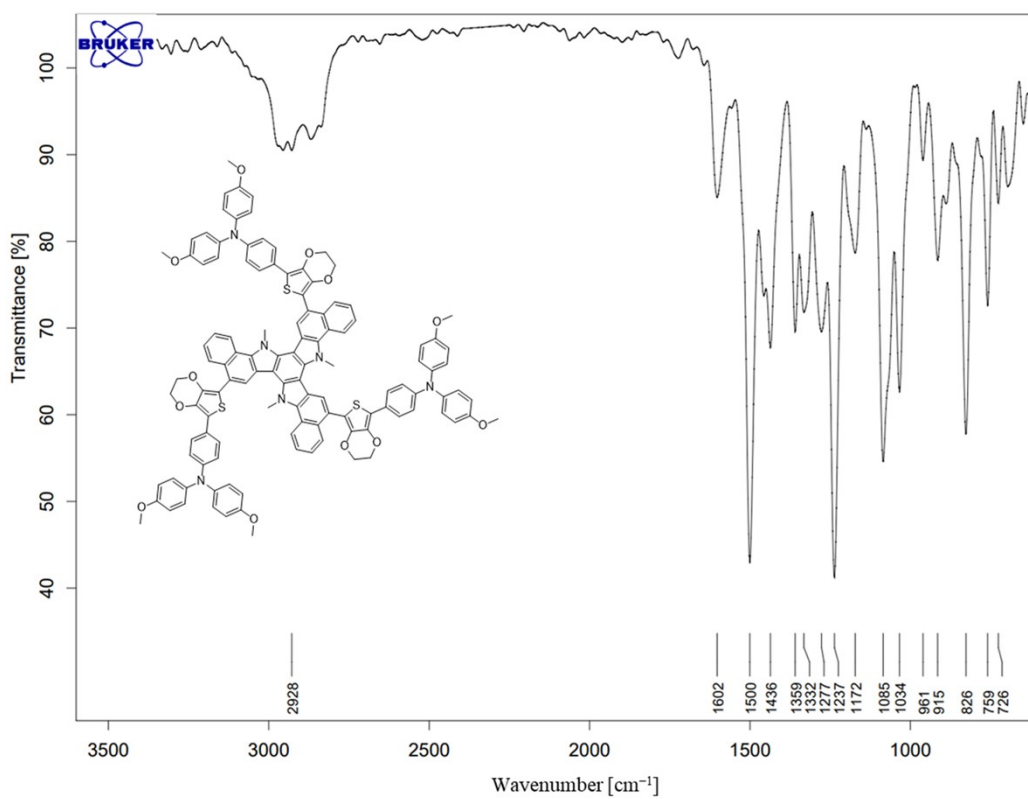**Fig. S33** ^{13}C NMR (101 MHz) spectrum of TBTAT-B-C1-e3 in THF-d_8.

Fig. S34 HR-MS of TBTAT-B-C1-e3.

Fig. S35 ATR-FTIR of TBTAT-B-C1-e3.